

# Hyperspectral Image Analysis for Automatic Detection and Discrimination of Residual Manufacturing Contaminants

Ava Vali

*Department of Electronics,  
Information and Bioengineering  
Politecnico di Milano  
Milan, Italy  
ava.vali@polimi.it*

Philipp Krämer

*Siemens AG - Technology  
LMU-Munich - Geosciences  
Munich, Germany  
kraemerphilipp@siemens.com*

Rainer Strzoda

*Siemens AG - Technology  
Munich, Germany  
rainer.strzoda@siemens.com*

Sara Comai

*Department of Electronics,  
Information and Bioengineering  
Politecnico di Milano  
Milan, Italy  
sara.comai@polimi.it*

Alexander M. Gigler

*Siemens AG - Technology  
LMU-Munich - Geosciences  
Munich, Germany  
alexander.gigler@siemens.com*

Matteo Matteucci

*Department of Electronics,  
Information and Bioengineering  
Politecnico di Milano  
Milan, Italy  
matteo.matteucci@polimi.it*

**Abstract**—In modern manufacturing, divergent market dynamics impel companies to move toward a zero-defect production by reducing the risk of errors and defects down to zero. Paint-coating of metal surfaces is one of such process steps and most prominent as consumers will be animated to buy based on their first impression. Despite significant advances in automation and precision engineering of paint-coating, the presence of process contaminants as residual of different stages of production may compromise the process. In this contribution, we focus on the paint-coating of washing machine cabinets as a representative. Within the last decade, hyperspectral imaging technology has shown promising potentials in a variety of applications that aim at detecting objects and discriminating materials. In this work, we present a hyperspectral acquisition and analysis system that verifies the feasibility of detection and discrimination of process contaminants smeared on the washing machine cabinet based on spectral information. The acquisition system, aided by a robot arm, collects hyperspectral images based on two scenarios: contaminants on flat steel sheets and contaminants on washing machine chassis. This dataset, which is published publicly, is calibrated, analysed, and segmented through the proposed analysis models. The results for both flat base and structured washing machine surfaces indicate the great capacity of this technology for being integrated into the pre-treatment stage before painting metal parts.

**Index Terms**—hyperspectral imaging, zero-defect manufacturing, process residual contaminants, contaminant discrimination, foreground extraction, image segmentation

## I. INTRODUCTION

Fast-changing customer's demands, volatility in local and global economics, and yet achieving success and profit in competitive markets has led companies to aim at reducing the risk of misproduction. Preventing defects and keeping errors

from becoming defects is a crucial task in realizing this goal. Zero-Defect Manufacturing [1] is a concept for this quality and production control to realize manufacturing with (close to) zero defects. The presence of residuals of different production stages as contaminants is one of the issues that currently leaves the production of painted metal parts with difficult compromises. In particular, maintaining the coating quality of paint in the production of washing machine cabinets is critical to keep it from corrosion and to provide a clean look. Yet, it is highly affected by these residual contaminants. Automatic detection and measuring of these residual contaminants before the painting stage is a significant step toward zero-defect manufacturing.

Hyperspectral Imaging (HSI) is a technique that combines conventional imaging with optical spectroscopy to sample spatially resolved spectral information from an object. HSI produces images in two spatial dimensions where each pixel carries spectral information (typically within a spectral range from visible to mid-infrared spectrum) that generates the third dimension of the image. Hence, such images are often called hyper-cube data or cubic images. Chemical sensitivity can be achieved towards the infrared region of the spectrum. As a rule of thumb, the chemical sensitivity and specificity enhance as wavelength increases, but at the same time capital expenditures for the systems increases. Near- or short-wave-infrared systems usually allow for sufficient chemical information at a reasonable price, but this of course strongly depends on the use-case. In the last decade, the concurrence of advances in HSI technologies and computational capacities has introduced hyperspectral sensors to new domains and applications. Besides the remote sensing field [2], where HSI

knowledge originated, there has been growing interest in HSI technology in diverse fields such as in industry [3], agriculture [4], food quality and safety [5], pharmaceuticals [6], and healthcare [7].

The significant advantages of hyperspectral images stem from the fact that besides containing the proper information to detect objects, they allow also the identification of the material by their different spectral absorption characteristics. In other words, the interaction of constituent molecules with different electromagnetic wavelengths demonstrates the material characteristics, which can lead to its identification and discrimination. For many organic molecules, such as oil and grease, these interaction wavelengths are accessible in the (near-)infrared region. Within the last decade, the food industry has significantly benefited from this information to detect ripeness or firmness of fruits [8], and to control the quality and safety of meats [9]. Such achievements made the potentials of HSI technology be recently noticed for the detection of contaminants in the manufacturing of metal parts and led to a new research trend on this emerging topic. In this work, we present the remarkable potential of this technology in detecting organic contaminants that are left throughout the different stages of the production of washing machine cabinets. The possibility of automatically eliminating defects before the painting stage allows moving toward the zero-defect manufacturing goal.

Proper analysis of hyperspectral images and the extraction of information come with a set of challenges. Some challenges are related to the type of data such as the so-called ‘curse of dimensionality’ (i.e., due to the high dimensionality of data) and redundancies within the data. In other words, the hyperspectral image comes with plenty of spectral information that does not contribute to the identification task, instead they complicate the analysis process dramatically. Machine learning has shown promising potentials in dealing with such complexity in hyperspectral image classification/segmentation. The work in [10] gives a brief introduction to machine learning techniques that are used for the classification of hyperspectral images. According to [10], Support Vector Machine (SVM), Random Forest (RF), and perceptron-base (Deep learning) techniques are the most common approaches in classifying hyperspectral images. In addition to the aforementioned techniques, in this work we examine K-Nearest Neighbor (KNN), Adaptive Boosting (AdaBoost), Gaussian Naive Bayesian (GaussianNB), Logistic Regression (LR), and Quadratic Discriminant Analysis (QDA) classification techniques to enable a wider comparative basis.

Another challenge in identifying contaminants on the chassis of washing machine cabinets is bound to direct reflections and to the presence of spatial and spectral noise. Since the surface is structured this adds complexity to the background. Therefore, both distinguishing the foreground and removing the unnecessary background not only lighten the burden of the computation but also help the machine to better process data. In [11], authors apply a spatial-spectral approach for the foreground (bacteria colonies) segmentation from the background (agar substrate). In this method, the map resulted by applying

foreground thresholding techniques is used together with the spectral cosine distance map of the hyperspectral image to finely segment bacteria from the background. The cosine distance map could be useful in determining the thickness of contaminations. However, in our study, we only focus on the localization of the contamination as well as contamination type discrimination.

To extract the foreground in hyperspectral images, the authors of [12] suggest an ensemble model consisting of a set of parallel and identical background subtraction models [13], each applied on a single spectral band. The foreground areas intersecting or overlapping with the majority of channels are subsequently considered the final foreground result. In this approach, the ground-truth is based on a-priori knowledge on background, meaning that the background can be modelled and the foreground is questioned. In our study, although the background is always the metal chassis, due to the variation of acquisition profiles in our dataset, it is difficult to model it precisely. Therefore, we propose to use a model for the extraction of the foreground inspired by the approaches proposed in [11] and [12]. In our model, the foreground thresholding technique is applied to each spectral band within an ensemble structure, and areas with more than a certain number of channel intersections are considered as foreground.

In this study, we investigate the potential of HSI technology in the detection of contaminants on metal chassis of washing machine cabinets by designing and implementing an acquisition and analysis system. As explained earlier, in our experiments we employ several machine learning techniques together with an ensemble feature extraction model. The goal of this experiment is to establish if the implementation of HSI technology for extracting process contaminants is feasible, suitable, and time-effective in the production line.

## II. METHODS

### A. Hyperspectral image acquisition

For our study, we designed and setup a HSI system based on a state-of-the-art hyperspectral push broom camera, Specim FX17, by SPECIM, Spectral Imaging Ltd. This type of camera features an optical imaging spectrograph in front of a two-dimensional optical detector array, resulting in a line imaging device where spatial information from a line in the scene is projected onto one dimension of the detector, while spectral information along this line is projected onto the other dimension of the detector, see figure 1. The Specim FX 17 addresses the spectral range between 900 nm and 1700 nm and captures images, co-registering 224 spectral channels with nominal 8 nm FWHM for each of its 640 ( $\times$  1) pixels sampling the line. In our scenario, broad band illumination of the sample is realized by a controlled artificial light source. We utilized a Metaphase UL Line Light by Metaphase Technologies Inc, which is a collimated array of 5 types of LEDs with their emission wavelengths centered at 1050 nm, 1200 nm, 1300 nm, 1450 nm and 1550 nm, respectively. The light source has gap less spectral coverage between 900 nm and 1700 nm and is a perfect match for the camera.

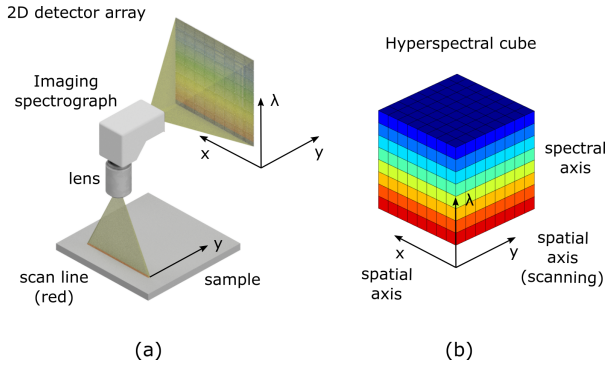


Fig. 1. Hyperspectral image acquisition: (a) schematics of a hyperspectral push broom scanner and the (b) corresponding orientation of the hyperspectral datacube. The cube is acquired by capturing frames  $(x, \lambda)$  while scanning along the  $y$ -axis. (not drawn to scale)

Since the push broom camera is capturing one spatial and the spectral dimension, the acquisition of a hyperspectral cube requires spatial scanning by relative lateral motion between the camera system and the sample. In contrast to common implementations of HSI push broom systems for industrial applications that use linear stages or conveyor belt systems for the motion, we mounted the camera and the light source on a convey robot arm as shown in figure 2. The robot was programmed to guide the optical system along a trajectory in a plane parallel to the sample surface with a constant offset of 249 mm, which equals the working distance of the optics. To scan one side of the chassis, we performed three consecutive line scans as we did not modify the existing camera nor the illumination setup. The surface was scanned at a speed of 100 mm/s by moving the optical system over the sample in a zigzag pattern schematically shown in yellow lines: along the solid lines the camera records data and along the dashed lines it returns back to the starting position of the next scan.

The data acquired from the three scans was concatenated into a single hyperspectral cube file for each run. We captured our images at 10 ms and 20 ms integration times for later analysis of the trade-off between the S/N ratio at low intensities and potential photo detector non-linearities at high intensities (in the best cases the camera corrects this non-linearity internally). The complete dataset is published in [14].

### B. Hyperspectral image analysis

The overall configuration for the implementation of the image processing chain is shown in Fig.3. This configuration comprises a data preparation, a foreground extraction, and a classification stage. Data preparation is the primary step, which is determined by the acquisition profile and the size of the acquired hyperspectral image. The aim of this stage is to adjust and calibrate data in a way that it is visually perceivable and easier for the machine to process. In the foreground extraction stage, the prepared data are processed to eliminate the unwanted background. This includes a pre-processing step that helps with better identification of the foreground and an

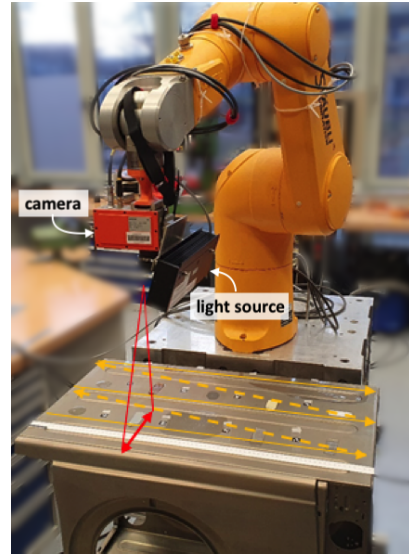


Fig. 2. The hyperspectral acquisition system setup. The camera and the broadband light source are mounted on a convey robot arm. To capture the entire surface, the robot arm moves on a path schematically shown in yellow. The scan width of the camera is schematically depicted as a bold red arrow. (Note: the image shows the arm in its park position, therefore the distance from the surface is not the acquisition distance.)

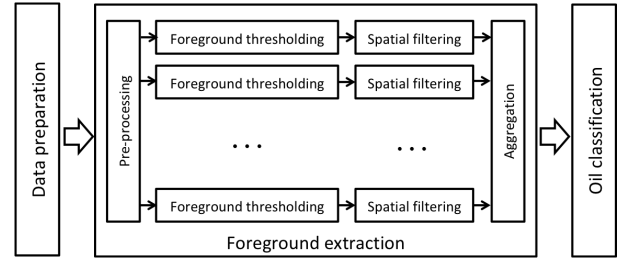


Fig. 3. The experiment chain, including data preparation, foreground extraction and classification stages. In the foreground extraction stage, after an internal pre-processing step, an ensemble model is employed within which each channel is processed independently, then all extracted foregrounds per channel are aggregated as the final foreground.

ensemble model that is designed to first extract the foreground-background map and, subsequently, eliminate the background regions of the hyperspectral image from the data preparation stage. Within the contaminant classification phase, stratified sampling is applied to the data using the ground-truth to split it into sets for training, validation, and testing. Around one-third of the pixels in the dataset are kept out as test data in order to provide an evaluation of all final models. The rest of the samples is used to train the models and to tune the hyper-parameters using k-fold cross-validation.

To improve the accuracy of reflectance transformations and tampering the effect of variations in illumination profile, white-dark calibration is performed as a part of the data preparation stage. The white (100% illumination of a Lambertian reflector) and dark (shutter is closed) reference hyperspectral images determine the maximum and minimum values of reflectance at each pixel position. Therefore, by

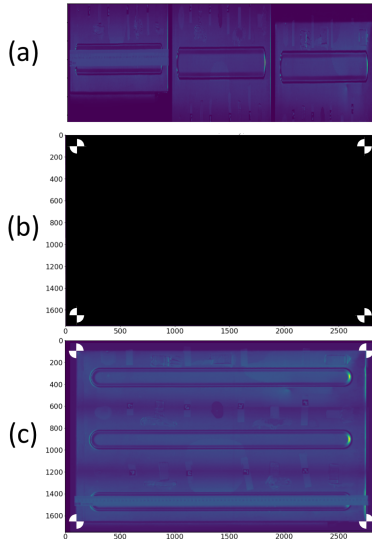


Fig. 4. Reshape and resizing the hyperspectral image. (a) Image before reshaping and resizing, (b) Size-reference image, (c) Hyperspectral image after being reshaped and resized to be matched with the size-reference image.

calculating the actual reflectance  $R$  using  $R = \frac{I-D}{W-D}$ , where  $I$  is the non-calibrated hyperspectral image and  $W$  and  $D$  are the white and dark references, respectively, the spectral information becomes independent from spatial and temporal variation in the illumination profile. In the experiment on the whole chassis, the reference ceramics did not cover the whole field of view (line) of the camera, therefore we replicated the closest pixel values for the missing ones. Yet, it resulted a noisy reflectance shift (slightly darker) around 5% of the length at both ends of the reference line (as can be observed in Fig.4-a).

We then reshape and resize the images to match their actual spatial width-height proportion. In the case of whole chassis image, the acquisition system produces three images (Fig.4-a). These images are reordered and matched by the edges to generate the whole. Then, a feature-based image alignment technique is applied to resize the image to match the size-reference image (Fig.4-b). The size-reference image contains four markers that indicate the outer corners of the chassis surface. By extracting the outer corners of the hyperspectral image and aligning them with the size-reference image's corner points using a homography transformation, the whole image can be resized into its actual proportion.

To achieve an accurate foreground segmentation, the Adaptive Histogram Equalization (AHE) method is used to improve image contrast locally, during the feature extraction pre-processing step shown in Fig.3. AHE is also helpful in amplifying noise in homogeneous regions of the image, making it easier to detect possible noises (as shown in Fig.5). Therefore, using AHE prior to noise-removal filters increases the chance of removing unwanted noise within the image. For pre-processing noise-removal, we apply a Median Filter with a  $10 \times 10$  window per channel. We consider outlier reflections, regular random image noises, unimportant scratches and tiny

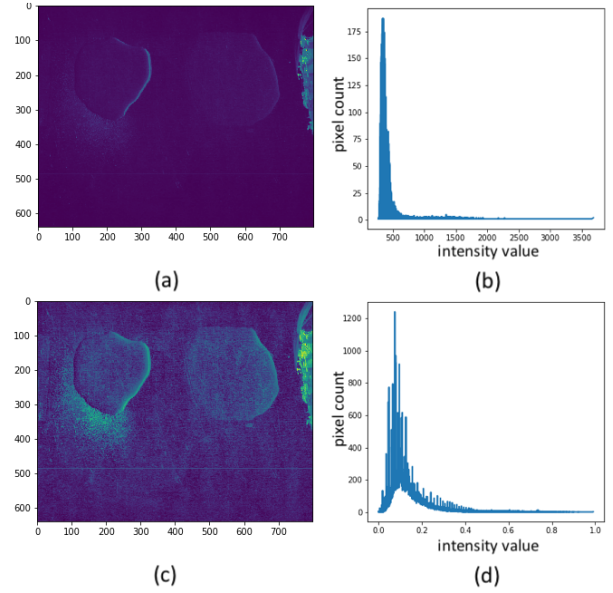


Fig. 5. An example demonstrating the effect of AHE in increasing the contrast and amplifying the noises, visualized for one channel. (a) and (b) are the original image and its histogram for one channel, respectively; (c) and (d) visualize the effect of AHE. Note: for the sake of a clearer presentation in the histograms, zero intensity is excluded. The high proportion of pixels with zero value obscures the distribution of foreground pixels in the histograms.

details as noises. Therefore, due to their size, a window size smaller than  $10 \times 10$  cannot properly conduct the noise removal task.

The foreground extraction stage comprises an ensemble model, which consists of identical foreground thresholdings followed by spatial filterings per channel. The stage is then concluded by aggregating the obtained results as the final foreground. In foreground thresholding, pixels with intensities within a range defined by threshold(s) are assumed as the foreground. In this experiment we tested: channel's mean value as a single threshold ( $FG = [I \geq \mu(I)]$ ) and different proportions of standard deviation from the mean as foreground intervals ( $FG = [\mu(I) - c\sigma(I) \leq I \leq \mu(I) + c\sigma(I)]$ ). After primary tests, we chose mean thresholding for the experiment as it showed more accurate foreground segmentation. Subsequently, we apply another median filter to remove noises in the thresholding step and a sequence of closing and opening morphological filters to ensure the continuity of the foreground areas. We chose circular masks with a diameter between 10 and 14 pixels for both closing and opening filters empirically. The effect of median and morphological filters on thresholded foreground is shown in Fig.6. In the aggregation step, per-channel foregrounds are aggregated in such a way that the areas with at least 15% of channels intersection are accepted as foreground and the rest are ignored as background.

The contaminant classification step is conducted using different linear and nonlinear supervised classifiers. As listed earlier, SVM (linear and non-linear), RF, Multilayer Perceptron (MLP), AdaBoost, KNN, GaussianNB, LR, and QDA methods are chosen as classifiers to provide a wider comparative basis

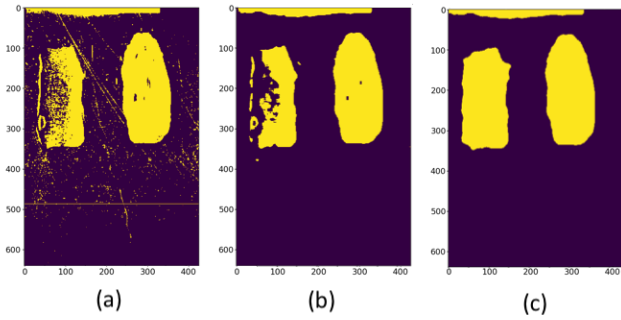


Fig. 6. An example demonstrating the effect of median and morphological filters in enhancing the thresholded foreground for one channel. (a) is the foreground obtained using mean threshold. (b) displays the effect of the median filter in removing the noise in (a). (c) shows the effect of closing and opening morphological filters on realizing the continuity of regions in (b).

for this study. SVM with linear kernel has been widely used with success for classification of hyperspectral images. In this study, we also examine SVM with nonlinear Radial Basis Function (RBF) kernel. RF (with 200 estimators), Adaboost (with 200 estimators), and KNN (with  $k = 3$ ) are other powerful non-parametric classifiers picked out for this experiment. The perceptron-based classifiers, such as MLP, have shown promising performance in classifying hyperspectral images when there exists an enormous amount of labeled data for training. In our experiment we test the MLP classifier with 100 hidden neurons, once arranged in one layer and once in two layers (each layer contains 50 neurons), and the “adam” optimizer. LR and GaussianNB are two popular probabilistic classifiers chosen for this experiment, which are, respectively, linear and non-linear. QDA is another non-linear probabilistic classifier useful to understand if individual classes have distinct covariances.

### III. RESULTS

We analysed up to 10 different organic contaminant substances, once placed on a flat steel sheet and then on a washing machine chassis (not flat, containing reinforcing ribs). These types of contaminants are determined by the materials used in the production of the washing machine cabinet during coil cutting, stamping and welding stages. Fig.7 displays the spectral signatures of all contaminants used in the experiment. The spectral signatures of these contaminants distinctively differ and this helps with proper discrimination.

The foreground extraction stage exhibits remarkable performance in removing the unwanted background with flat steel surface. Fig.8 visualizes an example of foreground extraction of four contaminants on a flat steel sheet: (a) is one channel of the hyperspectral image after AHE, (b) is the aggregated foreground-background map, and (c) is a 3D visualization of the foreground of the hyperspectral image. However, for the chassis sample the areas with the reinforced ribs reflect the light directly to the camera causing signal shifts that result in outlier pixels of high intensity in the captured image. Accordingly, the proposed thresholding technique does not

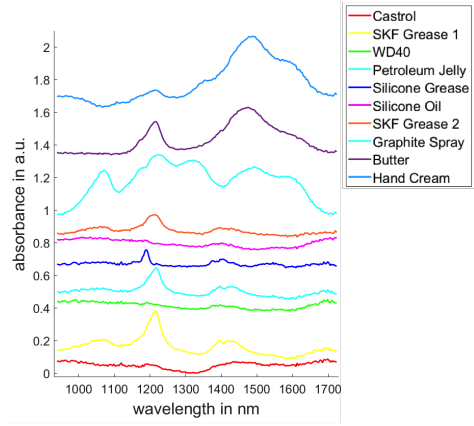


Fig. 7. Spectral signatures of the ten organic contaminants used in the experiment. The x and y axis correspond to the wavelength in  $nm$  and absorbance in  $a.u.$ , respectively. Note: for visual discrimination of the spectral features all the signatures are plotted with an individual offset.

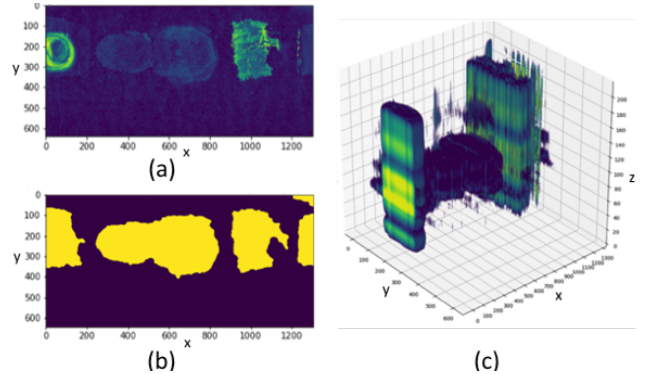


Fig. 8. An example showing the result of foreground extraction of a hyperspectral image consisting of four types of contaminants on a flat steel background. (a) shows one channel of the hyperspectral image after AHE, (b) shows the aggregated foreground-background map (foreground in yellow and background in purple), and (c) shows the hyperspectral image in 3D after removing the background pixels indicated in (b).  $x$  and  $y$  are the spatial axes,  $z$  is the spectral axis.

perform well in the case of not-flat surfaces. To proceed with the experiment, we do not apply the foreground extraction stage on the chassis sample, but we directly pass it to the contaminant classification stage to understand how the classifier distinguishes the foreground oils from other unwanted background pixels.

The ground-truth is assembled through a semi-manual process, which samples  $50 \times 50$  pixels of each contaminant (in resized version). To provide the machine with a clue on background features, we also sample  $50 \times 50$  pixels as unwanted background. For the experiment with flat steel sheets, we analysed 6 types of contaminants. For the classification, the ground-truth is randomly split for training and cross-validation in 5 folds (80/20 proportion). The classifier includes standardization to provide a comparable scale for features. For hyper-parameters optimization of the classifiers, we used grid search, and the results we provide here belong to the best estimator (estimator with the best parameters), which is

TABLE I  
CLASSIFIERS PERFORMANCE ON THE 6-TYPES-OF-CONTAMINANTS

Classifier	Cross-validation			Test		
	Prec.*	Rec.*	F1*	Prec.	Rec.	F1
<i>SVM-Linear</i>	0.9844	0.9841	0.9841	0.9720	0.9703	0.9702
<i>SVM-RBF</i>	0.9751	0.9743	0.9743	0.9638	0.9604	0.9602
<i>RF</i>	0.9721	0.9717	0.9717	0.9545	0.9522	0.9521
<i>MLP</i>	0.9625	0.9606	0.9606	0.9776	0.9774	0.9773
<i>LR</i>	0.8850	0.8789	0.8774	0.8815	0.8746	0.8734
<i>KNN</i>	0.7240	0.7125	0.7138	0.7419	0.7451	0.7393
<i>GaussianNB</i>	0.7140	0.7198	0.7133	0.6728	0.6866	0.6745
<i>AdaBoost</i>	0.6802	0.6567	0.6314	0.6328	0.6249	0.5812
<i>QDA</i>	0.6068	0.2198	0.1940	0.6419	0.6449	0.6242

The ordering is based on cross-validation mean precision

\* Mean of the k-fold

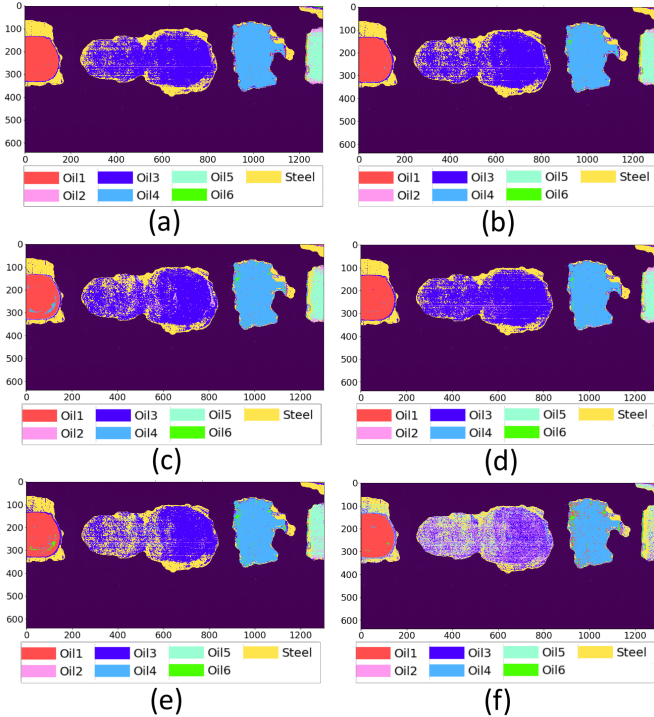


Fig. 9. An example of how different estimators perform in segmenting the foreground, which is already extracted using the foreground extraction mechanism, based on a hyperspectral image captured from a flat sheet steel smeared with four types of process contaminants. The segmented maps belong to: (a) SVM-Linear, (b) SVM-RBF, (c) RF, (d) MLP, (e) LR, and (f) KNN.

chosen based on the mean cross-validation score calculated over the accuracy. Tab.I lists the precision, recall, and F1-score for each employed classifier through cross-validation and the final testing. Fig.9 demonstrates how 6 highest-precision fitted classifiers perform in segmenting a hyperspectral image where its background is eliminated by the foreground extraction model. For post-processing, a median filter can be applied to increase the regions cohesion within the segmented map.

For the hyperspectral images of the chassis, we increased the number of background samples in the ground-truth to include more of its variations. Therefore, to assemble the ground-truth for chassis images, we collected the  $50 \times 50$  pixels per

contaminant class and  $100 \times 1744$  pixels (two vertical scans with 50 pixels width) as background samples. These vertical scans include reinforcing ribs, unwanted borders, white-dark calibration noises, marking tape, and flat steel pixels. We considered four best-performing estimators in the case of flat steel sheets for the chassis experiment: SVM-Linear, SVM-rbf, RF, and MLP. To get the most out of the collected ground-truth, the number of folds for cross validation is increased to 10 (90/10 proportion for train and test), and the hyper-parameters are tuned using grid-search, similar to the flat sheet experiment. The mean precision, recall, and F1-score for the best estimators chosen by the grid-search through cross-validation and their final testing evaluation results are listed in Tab.II. The confusion matrix displayed in Fig.11 reveals how the trained SVM-RBF model, which is the best performing model, classifies the samples and which are the errors. Fig.10 shows how each of the above estimators performs in segmenting the foreground from the background and in discriminating the contaminants in a hyperspectral image sample that consists of 15 smears made using 10 different types of process contaminants. Although, within the confusion matrix, the graphite spray samples seem to cause the major confusions, the extracted foreground in Fig.10 exhibits no specific bias with respect to the other classes.

TABLE II  
CLASSIFIERS PERFORMANCE ON 10-TYPES-OF-CONTAMINANTS AND CHASSIS BACKGROUND

Classifier	Cross-validation			Test		
	Prec.*	Rec.*	F1*	Prec.	Rec.	F1
<i>SVM-RBF</i>	0.9247	0.9192	0.9121	0.9731	0.9807	0.9765
<i>MLP</i>	0.8962	0.8634	0.8557	0.9669	0.9657	0.9656
<i>RF</i>	0.8685	0.6717	0.7084	0.9454	0.8447	0.8871
<i>SVM-Linear</i>	0.8432	0.7786	0.7865	0.9073	0.8934	0.8915

The ordering is based on cross-validation mean precision

\* Mean of k-fold

#### IV. DISCUSSION AND CONCLUSION

We presented the design, implementation, and testing of a hyperspectral imaging system for detection and discrimination of organic contaminants which are residuals of different stages of the washing machine cabinet production. To examine the effectiveness and feasibility of this system and to collect objective knowledge, we established pilot experiments replicating the occurrence of some possible contaminants in controlled lab conditions. The experiment is conducted on the basis of two scenarios: the first is to analyse contaminants on small flat steel sheets, and the second is to analyse these contaminants on a real washing machine chassis featuring reinforcement ribs. The foreground extraction step proposed in the model did not act effectively for the hyperspectral images we captured based on the latter scenarios. This was due to the reflectance irregularity caused by the uneven surface and the white-dark calibration noises. Yet, just ignoring the foreground extraction step for the second scenario, in this work we established the

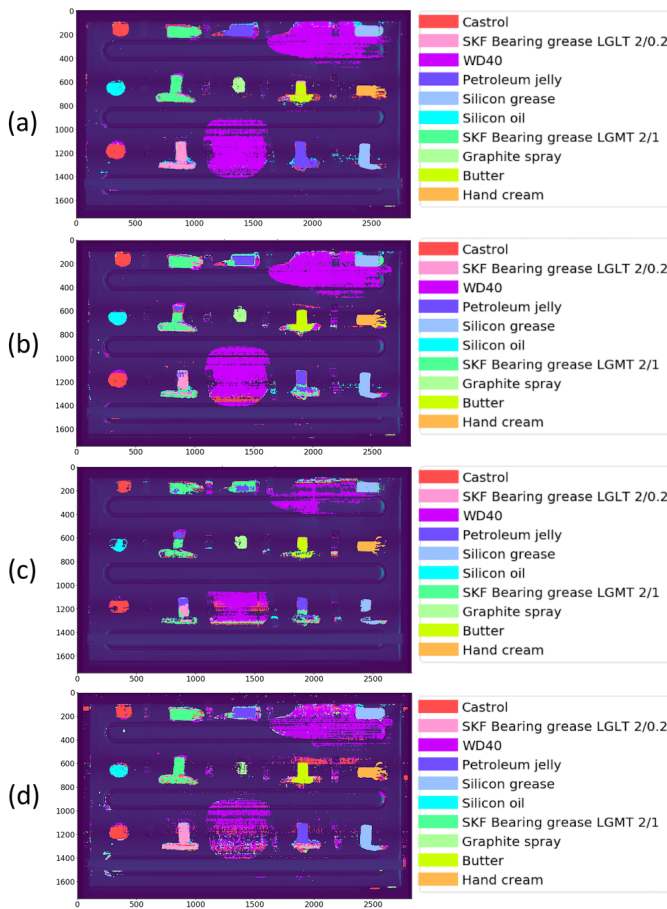


Fig. 10. The results of contaminant segmentation using different classifiers based on a hyperspectral image sample from the washing machine chassis smeared using 10 types of contaminants. For the sake of visibility, the pixels segmented as background are replaced with one channel of the actual hyperspectral image. The segmented maps refer to: (a) SVM-RBF, (b) MLP, (c) RF, and (d) SVM-Linear.

feasibility of a reliable system that can detect, localize, and discriminate organic contaminants using hyperspectral images.

Despite the remarkably short inference time (less than a second to discriminate contaminants within a full chassis image using a single AMD64 core), the designed acquisition process acts as the main time bottleneck because of calibration and the acquisition time. This study suggests further investigations over improving and adapting the acquisition lighting system to illuminate the entire surface of the washing machine cabinet at once. This not only shortens the time of the acquisition process but also decreases the acquisition noises. It helps with more precise calibration and more accurate segmentation, and increases the scalability of this solution for being integrated into the production line. Realizing the proper integration of the acquisition system within the production line and collecting real-time data offer the opportunity of a comprehensive model evaluation and generalizing the findings to real settings with uncontrolled variables.

In this study, 10 types of common organic contaminants were considered as the residuals of the production line. How-

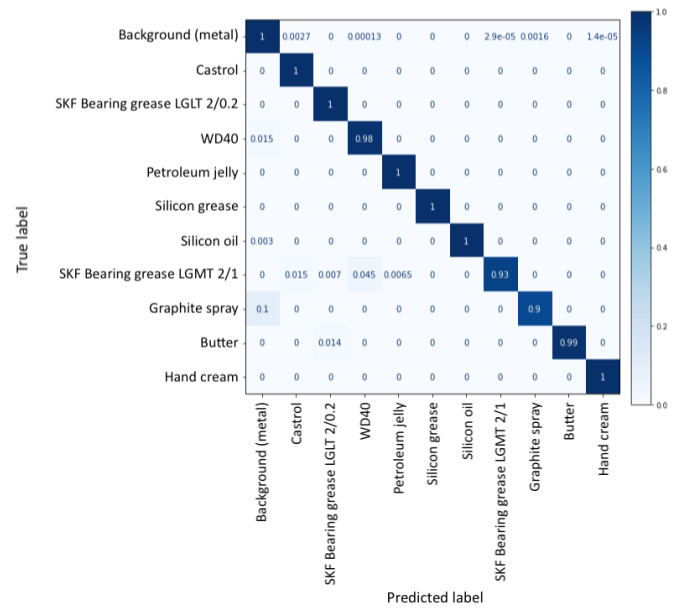


Fig. 11. The confusion matrix displaying the evaluation results using the test dataset on the trained SVM-RBF model. Given the fact that the ground-truth is not necessarily free of noise, this model exhibits remarkable performance in classifying contaminants.

ever, the arbitrary contaminants are yet possible to remain throughout the production stages, which calls for supplementary investigations. Furthermore, the assessment of contaminant thicknesses should be considered for further studies, as such information would significantly improve the cleaning process. Additionally, in the pilot experiments presented by this work, we do not consider the situation where the contaminants are mixed or have overlaps, which remains to be investigated in future works.

#### ACKNOWLEDGMENT

This work has been carried out under the *LoViCoSpec* project (Localization and Visualization of Contaminations in Manufacturing by Spectral Vision), supported by the *European Institute of Innovation & Technology* (EIT), as a part of the *EIT Manufacturing Mission 2020*. The authors would like to express their sincere thanks to Pierluigi Petrali and *Whirlpool-EMEA, Manufacturing R&D*, for coordinating this project, and Sven Dudeck, Peter Rentschler, Eric Arnold, and Christian Mose for their support in creation of the hyperspectral acquisition system and implementation on the robot arm.

#### REFERENCES

- [1] F. Psarommatis, G. May, P.-A. Dreyfus, and D. Kiritsis, "Zero defect manufacturing: state-of-the-art review, shortcomings and future directions in research," *International Journal of Production Research*, vol. 58, no. 1, pp. 1–17, 2020.
- [2] M. B. Stuart, A. J. McGonigle, and J. R. Willmott, "Hyperspectral imaging in environmental monitoring: a review of recent developments and technological advances in compact field deployable systems," *Sensors*, vol. 19, no. 14, p. 3071, 2019.
- [3] G. Bonifazi, R. Palmieri, and S. Serranti, "Evaluation of attached mortar on recycled concrete aggregates by hyperspectral imaging," *Construction and Building Materials*, vol. 169, pp. 835–842, 2018.

- [4] B. Lu, P. D. Dao, J. Liu, Y. He, and J. Shang, "Recent advances of hyperspectral imaging technology and applications in agriculture," *Remote Sensing*, vol. 12, no. 16, p. 2659, 2020.
- [5] H. Pu, L. Lin, and D.-W. Sun, "Principles of hyperspectral microscope imaging techniques and their applications in food quality and safety detection: A review," *Comprehensive reviews in food science and food safety*, vol. 18, no. 4, pp. 853–866, 2019.
- [6] J. Bøtker, J. X. Wu, and J. Rantanen, "Hyperspectral imaging as a part of pharmaceutical product design," in *Data Handling in Science and Technology*. Elsevier, 2020, vol. 32, pp. 567–581.
- [7] M. Halicek, H. Fabelo, S. Ortega, G. M. Callico, and B. Fei, "In-vivo and ex-vivo tissue analysis through hyperspectral imaging techniques: revealing the invisible features of cancer," *Cancers*, vol. 11, no. 6, p. 756, 2019.
- [8] G. A. Leiva-Valenzuela, R. Lu, and J. M. Aguilera, "Prediction of firmness and soluble solids content of blueberries using hyperspectral reflectance imaging," *Journal of Food Engineering*, vol. 115, no. 1, pp. 91–98, 2013.
- [9] M. M. Reis, R. Van Beers, M. Al-Sarayreh, P. Shorten, W. Q. Yan, W. Saeys, R. Klette, and C. Craigie, "Chemometrics and hyperspectral imaging applied to assessment of chemical, textural and structural characteristics of meat," *Meat science*, vol. 144, pp. 100–109, 2018.
- [10] A. Vali, S. Comai, and M. Matteucci, "Deep learning for land use and land cover classification based on hyperspectral and multispectral earth observation data: A review," *Remote Sensing*, vol. 12, no. 15, p. 2495, 2020.
- [11] S. Arrigoni, G. Turra, and A. Signoroni, "Hyperspectral image analysis for rapid and accurate discrimination of bacterial infections: A benchmark study," *Computers in Biology and Medicine*, vol. 88, pp. 60–71, 2017.
- [12] M. Shah, V. Cave, and M. dos Reis, "Automatically localising rois in hyperspectral images using background subtraction techniques," in *2020 35th International Conference on Image and Vision Computing New Zealand (IVCNZ)*, 2020, pp. 1–6.
- [13] B. Garcia-Garcia, T. Bouwmans, and A. J. R. Silva, "Background subtraction in real applications: Challenges, current models and future directions," *Computer Science Review*, vol. 35, p. 100204, 2020.
- [14] B. A. M Graña, MA Vezanzons, "Near infrared hyperspectral image data of organic surface contaminations," May 2021, This dataset was created within the EIT-M funded project LoViCoSpec in 2020. [Online]. Available: <https://doi.org/10.5281/zenodo.4736803>